Actomyosin controls planarity and folding of epithelia in response to compression

Tom P. J. Wyatt[1,2,8], Jonathan Fouchard[1,8], Ana Lisica[1], Nargess Khalilgharibi[1,2], Buzz Baum [3,4]*, Pierre Recho [5,6], Alexandre J. Kabla [6]* and Guillaume T. Charras [1,4,7]*

Throughout embryonic development and adult life, epithelia are subjected to compressive deformations. While these have been shown to trigger mechanosensitive responses such as cell extrusion and differentiation, which span tens of minutes, little is known about how epithelia adapt to compression over shorter timescales. Here, using suspended epithelia, we uncover the immediate response of epithelial tissues to the application of in-plane compressive strains (5–80%). We show that fast compression induces tissue buckling followed by actomyosin-dependent tissue flattening that erases the buckle within tens of seconds, in both mono- and multi-layered epithelia. Strikingly, we identify a well-defined limit to this response, so that stable folds form in the tissue when compressive strains exceed a 'buckling threshold' of ~35%. A combination of experiment and modelling shows that this behaviour is orchestrated by adaptation of the actomyosin cytoskeleton as it re-establishes tissue tension following compression. Thus, tissue pre-tension allows epithelia to both buffer against deformation and sets their ability to form and retain folds during morphogenesis.

Epithelial tissues are frequently subjected to in-plane compression during adult life and embryonic development, as the result of both intrinsic and extrinsic forces[1–4]. These forces are central to the function of many organs and are crucial for sculpting complex tissue shapes during developmental morphogenesis[5–7]. For example, in the airway, epithelia are subjected to periodic area changes during normal breathing and to longer term compression during diseased states such as asthmatic bronchial contraction[8,9]. During embryonic development, compression guides a number of morphogenetic events involving tissue bending and folding, such as the formation of the optic cup[6], gut villi[7] and cortical convolutions in the brain[10].

Recent work has suggested that epithelia have evolved a variety of cellular-scale mechanisms to detect and respond to compression via mechanotransduction[11]. For example, compressive deformations can activate signalling pathways that regulate cell differentiation[3,12]. Moreover, cultured and primary epithelial monolayers can respond to increases in their density induced by compression by triggering the extrusion of live cells[13,14].

In vivo, epithelia are subjected to deformations lasting milliseconds to hours[15]. Yet, cellular-scale adaptive processes typically necessitate a period of hours. Whether and how epithelia respond to compression at shorter timescales is poorly understood. Although remodelling of the cell structure through biomolecular signalling cascades may be too slow to respond at the shortest of timescales, recent work has revealed rapid adaptive responses emerging directly from the mechanical properties and dynamic organization of actomyosin[16–18].

Here, to investigate the response of epithelia to compressive strain, we use suspended epithelia devoid of a substrate. This enables the study of the intrinsic response of the cells without mechanical interference from the extracellular matrix. We find that both mono- and multi-layered epithelia can accommodate compression up to a well-defined limit of $\sim-35\%$ strain, the buckling threshold. Up to this threshold, actomyosin-generated pre-tension allows the tissues to actively retain a planar morphology during slow compressive strains and erases buckles induced by faster strains within tens of seconds. Tissue tension decreases linearly with compressive strain, approaching zero at the buckling threshold, at which point stable folds are formed in the tissue. The observed tissue behaviours can be recapitulated by modelling epithelia as pre-tensed viscoelastic sheets that exhibit a buckling instability on entering compression. Finally, we show that the buckling threshold is determined by the ratio between tissue pre-tension and tissue elasticity, as predicted by a simple rheological model.
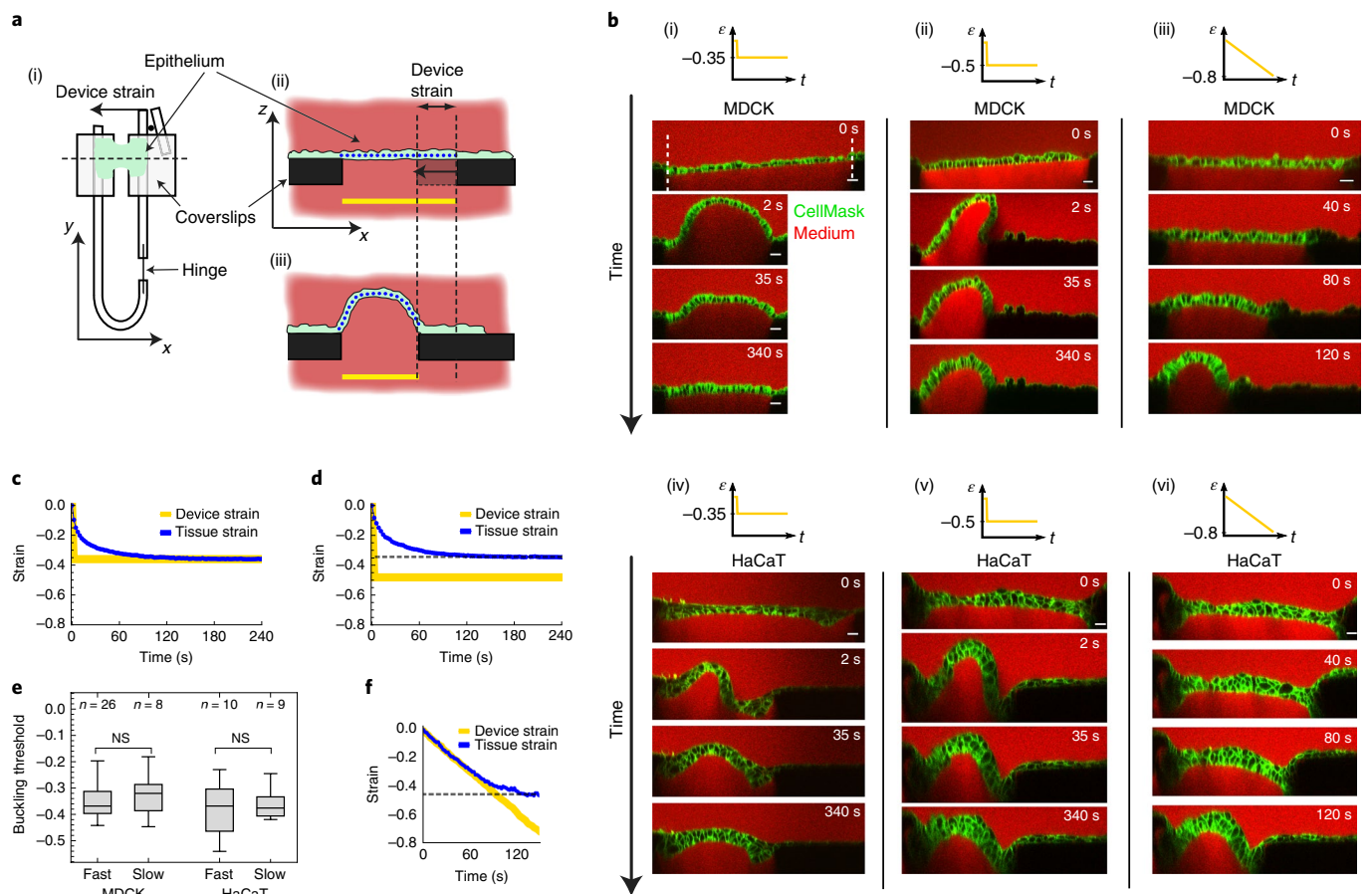
Results

Fast mechanical adaptation of epithelia to compression. To investigate the cell-intrinsic response of epithelia to compressive strains, we used cultured Madin–Darby canine kidney (MDCK) epithelial monolayers devoid of a substrate[19–21] (Fig. 1a). It is well understood from classical mechanics that slender elastic materials subjected to compressive strains will buckle, that is, they will undergo bending after a critical point. Here, after a step of −35% strain ('device strain', Fig. 1a) applied at high strain rate (500% s^{-1}), most suspended MDCK monolayers took on an arched shape (Fig. 1b(i) and Supplementary Fig. 1a(i)), reminiscent of buckling in solid materials. Less frequently, epithelia adopted a transient wave-like shape, similar to the second mode of buckling, before rapidly transitioning to the arched shape (Supplementary Fig. 1a–c and Supplementary Note 1).

Remarkably, the buckles were not stable configurations. Instead the epithelia rapidly erased buckles, becoming planar within ~1 min (Fig. 1b(i) and Supplementary Video 1). To quantify the evolution

Fig. 1 | Fast mechanical adaptation of epithelia to compression. a, Schematic diagram showing the method for application of compressive strain to suspended epithelia. (i), Top view of the mechanical manipulation device. Uniaxial strain is applied to the tissue (green) by displacing the flexible arm. (ii),(iii), Profile views of the setup along the dashed line in (i): an epithelium (green) is suspended between two coverslips (black) (ii) and the right-hand coverslip is displaced, deforming the tissue (iii). The yellow lines denote the distance between the coverslips from which the applied 'device strain' is calculated. The blue dotted lines denote the tissue contour length. **b**, Time series of profiles of epithelia before and during application of various compressive strains ε, applied at different rates. Strain was applied either as a step at high strain rate (500% s^{-1}, (i),(ii) and (iv),(v)) or as a ramp at low strain rate (0.5 % s^{-1}, (iii),(vi)): step of intermediate amplitude (−35%) (i); step of large amplitude (−50%) (ii) and strain ramp (−80%) (iii), applied to MDCK monolayers. (iv)–(vi), As in (i)–(iii) but for multi-layered HaCaT epithelia. Cell membranes are marked with CellMask (green), the medium is visualized using dextran Alexa-647 (red) making coverslips appear dark by dye exclusion. Scale bars, 20 µm. The number n of biologically independent repeats of the representative images and the corresponding data in **c,d,f** is n = 17, 26, 8, 7, 10, 9, from (i)–(vi). **c,d**, Temporal evolution of the tissue strain (blue) of an MDCK monolayer after a step of −35% device strain (yellow) (**c**) and −50% device strain (**d**). **e**, Comparison of the buckling threshold ε_b in MDCK and HaCaT epithelia measured following a fast step or a slow ramp of compressive strain. NS, not significant, P = 0.45, 0.65 for MDCK and HaCaT, respectively; Mann–Whitney U-test. The distributions' medians, first and third quartiles and ranges are represented by the central bars, bounding boxes and whiskers, respectively. The number of biologically independent experiments is given above each box plot. **f**, Temporal evolution of the tissue strain (blue) during a ramp of device strain (yellow). The dashed lines in **d,f** mark the maximum tissue strain, termed the buckling threshold ε_b.

of tissue strain, we extracted the contour length of the tissue cross section and compared it to its value before strain application (Supplementary Fig. 1d). Following application of a step of compressive strain, tissue strain first decreased rapidly before gradually slowing as the tissue approached a planar configuration (Fig. 1c). The average half-life of the flattening process was $T_{1/2}$ = 4.8 ± 0.8 s.

To determine the limit of this adaptive process, we applied a larger strain (−50%) at the same strain rate. The tissues exhibited the same initial flattening behaviour but could not completely accommodate the larger deformation (Fig. 1b(ii), Fig. 1d and Supplementary Video 2). As a result, a buckle remained that was stable for over 10 min (Supplementary Fig. 1e). Overall, the reduction of contour length after compression applied at high strain rate saturated at −34 ± 8% (Fig. 1e).

The presence of such a limit suggests that the tissue may possess a reference length, independent of time. To test this, the tissue strain was measured during a large compression applied at a low strain rate (80% at 0.5% s^{-1}). Here, the epithelium maintained a planar morphology for large deformations until taking on an arched shape, at which point its length did not decrease any further (Fig. 1b(iii), Fig. 1f and Supplementary Video 3). The maximum tissue strain here was −33 ± 8%, which was indistinguishable from the maximum deformation after fast application of compression (P = 0.45, Fig. 1e). Similar results were obtained when we sequentially applied a fast and slow deformation to the same monolayer with 6 min intervals (Supplementary Fig. 1f). This enabled us to define a tissue-intrinsic maximum strain, the buckling threshold ε_b, above which the tissue cannot decrease its contour length.

Interestingly, suspended multi-layered epithelia (HaCaT human keratinocytes) showed the same phenomenology (Fig. 1b(iv)–(vi), Supplementary Fig. 2a–d and Supplementary Videos 4–6) with a buckling threshold and average half-life of flattening indistinguishable from MDCK monolayers (Fig. 1e, $\varepsilon_b = -38 \pm 7$ %, $T_{1/2} = 2.7 \pm 0.7$ s, $P = 0.23$ and 0.07, respectively). Again, the buckling threshold did not depend on the loading regimen (Fig. 1e and Supplementary Fig. 1f). Therefore, the rapid response to compression is not specific to a particular cell type or tissue architecture and may be a generic property of epithelia. In addition, neither the half-life of flattening nor the buckling threshold correlated with cell density (Supplementary Fig. 2e,f). Thus, epithelial tissues rapidly adapt to large in-plane compressive strains by reducing their length up to a well-defined limit, the buckling threshold, which is independent of the history of deformation.

Tissue flattening depends on actomyosin contractility. To verify that cell-scale phenomena such as oriented divisions and extrusions are not involved in flattening, we acquired images of the cell-junction network before and after compression. The junctional network before compression could be recapitulated by applying a stretch equal to the applied strain to the image of the network after compression (Supplementary Fig. 3a). Thus, changes in cell shape alone account for the changes in tissue shape. In both MDCK and HaCaT tissues, compression led to a decrease in cell length along the axis of compressive strain (x) that closely matched the tissue deformation, while the cell length along the perpendicular (y) axis remained unchanged and cell height (z) increased (Fig. 2a,b and Supplementary Fig. 3b). In sum, the changes in cell shape fitted a model of constant cellular volume (Fig. 2b, dashed lines).

Since actomyosin activity drives both shape changes[22] and stress relaxation in single cells[23], we explored the role of actomyosin in tissue flattening. For this, we repeated the compression experiments in the presence of inhibitors of actomyosin. While all tissues still buckled on fast compression, flattening was severely compromised (Fig. 2c(i),d, Supplementary Fig. 3d,e and Supplementary Video 7). Firstly, consistent with the role of actomyosin in driving stress relaxation, the rate of flattening was reduced by inhibition of contractility (Fig. 2d and Supplementary Fig. 3d–g). Secondly and more surprisingly, the tissue's ability to accommodate strain saturated at smaller values (Fig. 2d,e), showing that the buckling threshold itself depends on actomyosin. Conversely, increasing contractility with calyculin A, a phosphatase inhibitor known to increase myosin II activity, increased tissue flattening rate and buckling threshold (Fig. 2d,e and Supplementary Fig. 3g). In addition, HaCaT multilayered epithelia showed the same response to inhibition of contractility as MDCK (Fig. 2c(ii),e and Supplementary Fig. 3g,h).

These results suggest that actomyosin activity not only permits the rapid adaptation of epithelia to compressive strain but also sets the buckling threshold, controlling the transition between planarity and folding in response to long-lasting compressive deformations.

Tissue pre-tension buffers against compression to prevent buckling. While buckling occurs under compressive stress in inert materials, epithelial tissues in vivo and in vitro are often actively pre-tensed by the actomyosin cytoskeleton[17,24,25]. We therefore hypothesized that actomyosin could tune the buckling threshold by controlling the magnitude of pre-tension. To test this, we measured pre-stress in MDCK monolayers (Fig. 3a). We found that pre-stress in control conditions was tensional with a magnitude of 240 ± 30 Pa (Fig. 3b), which is close to values measured via monolayer stress microscopy[26]. This pre-tension decreased dramatically with inhibition of contractility and increased when myosin activity was increased (Fig. 3b). Thus, pre-tension generation requires actomyosin and changes in the buckling threshold caused by actomyosin perturbation (Fig. 2e) were accompanied by changes in tissue pre-tension.

To characterize how tissue stress evolved during compressive strain, we applied a slow deformation to the tissues (as in Fig. 1f) whilst measuring the tissue-level tension (Fig. 3c and Methods). Tissue stress initially decreased linearly with strain, before transitioning, at a stress of 13 ± 4 Pa, to a second phase in which stress plateaued close to zero Pa (Fig. 3d, yellow). Such a stress–strain curve is a typical signature of a thin elastic sheet with a small bending modulus experiencing a buckling instability[27]. In support of this, the transition between the two phases occurred for a device strain of -33 ± 8% (Fig. 3d, dashed line, and Fig. 3e), which is indistinguishable from the buckling threshold identified by imaging ($P = 0.53$, Fig. 3e). This transition point remained stable over multiple compression cycles (Supplementary Fig. 4a,b) and when several minutes of stretch preceded compression (Fig. 3d, orange). These data further suggest that the buckling threshold is an intrinsic mechanical feature of the tissue to which we can associate a reference length.

Next, we measured the evolution of tissue stress in response to rapid steps in compressive strain of various magnitudes (2–65%). Stress always decreased immediately on application of compressive strain; however, for all but the largest strains, stress was rapidly re-established (Fig. 3f). Stress then plateaued at a level that depended on the magnitude of compressive strain applied, with a larger fraction of the pre-tension recovered after smaller strains (Fig. 3f). The curve relating steady-state stress to strain magnitude in high-strain-rate experiments closely matched the stress response observed during slow strain application (compare Fig. 3g,d). Indeed, the fraction of recovered stress decreased linearly with increasing compressive strain up to a transition point at a device strain of ~ -33%, below which there was no stress recovery (Fig. 3g).

Thus, the steady-state stress in MDCK monolayers evolves linearly with compressive strain, independently of the history of deformation, and planar tissue morphologies can only be maintained when this steady-state stress is tensional.

Epithelia behave as pre-tensed viscoelastic materials. These findings demonstrate that there exists a quasi-static regime in which the tissue behaves as a pre-tensed elastic sheet with negligible bending stiffness. Additionally, the timescales of tissue flattening (Fig. 1) and tension recovery (Fig. 3) suggest that a viscous contribution damps the response. To test this, we devised a simple rheological model consisting of a standard linear solid (in line with ref. [19]) in parallel with an active pre-tension element (Fig. 4a and Supplementary Note 2). To account for the nonlinearity at the buckling transition, in accordance with Euler buckling theory, we also supplemented the model with a 'buckling condition' in the form of a loss of tissue stiffness when stress becomes negative (Fig. 4a and Supplementary Note 2A).

As observed in experiments, the assumptions of the model immediately imply that, on application of compressive strain, the tissue may either buckle or remain planar, depending on the applied strain and strain rate (Supplementary Fig. 5a and Supplementary Note 2F). For example, when deformation below the buckling threshold is applied at sufficiently high strain rate, the tissue transiently buckles (as in Fig. 1b(i)). Indeed, under these conditions, the spring-dashpot element in the model behaves elastically at short timescales and causes the tissue stress to transiently decrease to zero. Then, as the dashpot relaxes, stress recovers and the tissue flattens.

To test whether the behaviour of epithelia subjected to compressive strain can indeed be captured by such a mechanical model, we parametrized the model from experiments (Supplementary Note 3) and simulated a set of mechanical perturbations. The parameters σ_a and E directly predict a buckling threshold $\varepsilon_b = -\sigma_a/E$ (Supplementary Note 2). Indeed, at this strain, the elastic branch E is subjected to a stress equal to $-\sigma_a$, reducing stress to zero in the tissue. With E measured as 640 ± 80 Pa, the ratio predicts a value of -38% for the buckling threshold, in close agreement with
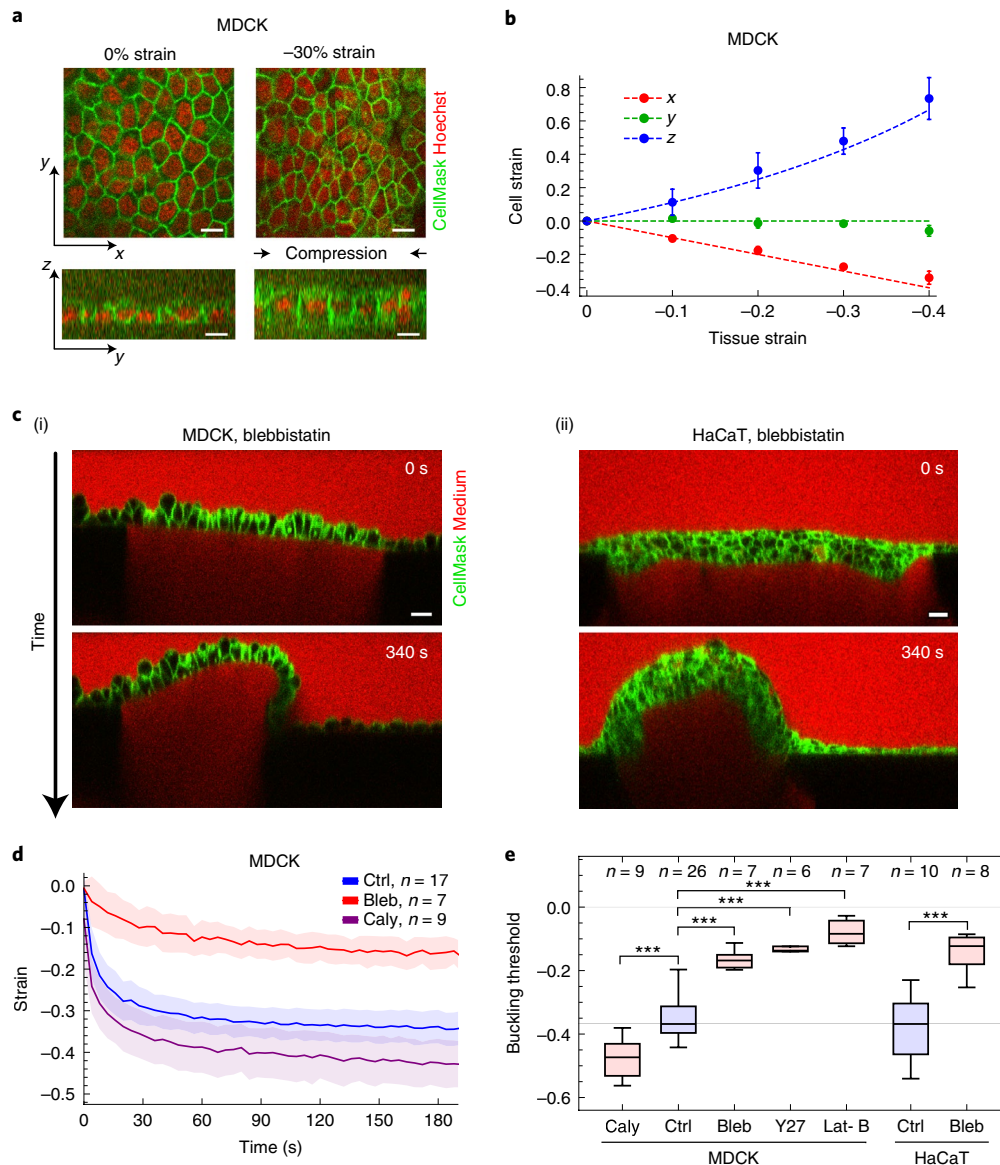
Fig. 2 | Tissue flattening is achieved through myosin-dependent cell shape change. a, Confocal images of MDCK epithelial monolayers before and during 30% uniaxial compressive strain. Plasma membranes are marked with CellMask (green) and nuclei with Hoechst-33342 (red). The x–y images are single confocal optical sections through the middle of the tissue. Compressive strain is applied along the x axis. Scale bars, 10 μm. The representative images in **a** and data in **b** are derived from $n=3$ biologically independent experiments. **b,** Cellular strain as a function of the strain applied to the MDCK tissues. Solid circles denote the mean cellular strain along the x axis (red), y axis (green) and z axis (blue). Error bars denote s.d. Dashed lines indicate the predicted cellular strain assuming that cell strain accounts entirely for tissue strain and that cells maintain constant volume during deformation by increasing their height (z). **c,** (i),(ii), Profile of an MDCK monolayer (i) and a HaCaT epithelium (ii) treated with blebbistatin (20 μM and 75 μM, respectively) and subjected to fast compressive strain. Scale bars, 20 μm. Time is indicated in the top right-hand corner. The number of biologically independent repeats of representative images shown in **c** is indicated above the box plots in **e**. **d,** Temporal evolution of tissue strain (mean ± s.d.) following fast compression for control (blue), blebbistatin (20 μM, red) and calyculin A (35 nM, purple) treated MDCK tissues. The number n of biologically independent experiments is indicated in the inset. **e,** Buckling threshold ε_b inferred from the maximal tissue strain reached after fast compression of MDCK and HaCaT epithelia. Tissues were treated with drugs altering actomyosin contractility. Caly, calyculin A (35 nM); Bleb, blebbistatin (20 μM for MDCK, 75 μM for HaCaT); Y27, Y-27632 (10 μM); Lat-B, latrunculin-B (3 μM). The distributions' medians, first and third quartiles and ranges are represented by the central bars, bounding boxes and whiskers, respectively. Statistically significant difference ***$P < 0.001$; Mann–Whitney U- test.

experiments (Figs. 1e and 3e). Furthermore, the model could accurately reproduce the temporal evolution of global tissue strain observed in experiments applying compressive strain at low strain rate (Fig. 4b). Simulations also accurately captured the different regimes of stress recovery after a fast step of compression (Fig. 3f, Supplementary Fig. 5c and Supplementary Note 2D), as well as the extent of this recovery as a function of applied compressive strain (Fig. 3g).

Epithelia possess short-term memory of past compression.
A further prediction of the model was that the time required for the tissue to flatten should depend on the history of deformation (Supplementary Note 2E). To test this experimentally, three cycles of 40% compressive strain were applied to the tissue at high strain rate (Fig. 4c). After each 6-min period of compressive strain, the tissue was returned to its original length for a chosen duration Δt (cycle 1, $\Delta t_1 = 3$ s; cycle 2, $\Delta t_2 = 6$ min).
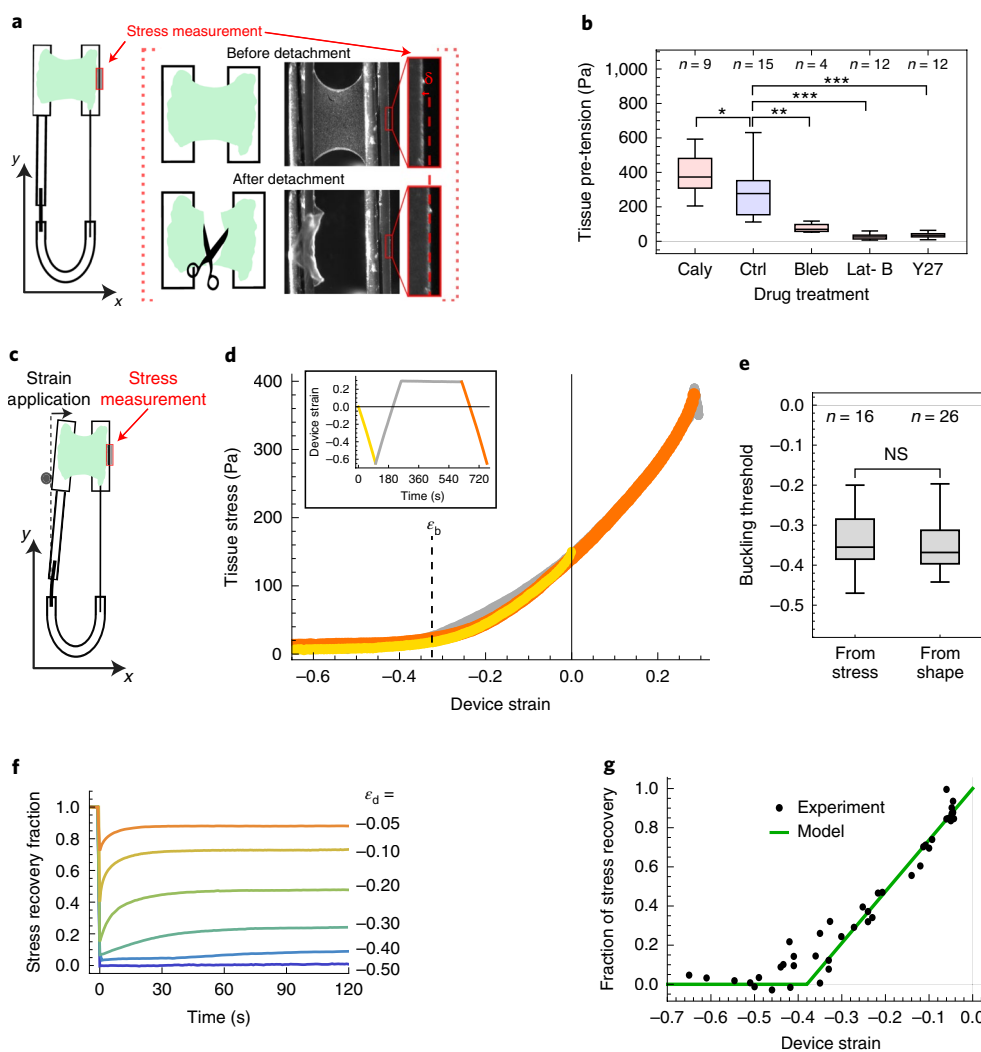
Fig. 3 | Pre-tension buffers against compression to prevent stable buckling of epithelia. a, Schematic diagram depicting the principle of measurement of pre-stress. The tissue (green) is cultured between a reference rod and a flexible rod. Measurement of the deflection of the flexible rod compared to its rest position allows determination of the stress applied by the epithelium. The deflection of the flexible rod δ is measured from bright-field images acquired before and after detachment of the tissue. $N = 17$ biologically independent replicates were obtained. **b**, Pre-tension of MDCK monolayers treated with drugs altering actomyosin contractility. Caly, calyculin A (35 nM); Bleb, blebbistatin (50 μM); Y27, Y-27632 (20 μM); Lat-B, latrunculin-B (3 μM). In **b** and **e** the distributions' medians, first and third quartiles and ranges are represented by the central bars, bounding boxes and whiskers, respectively. Statistically significant difference *$P < 0.05$; **$P < 0.01$ and ***$P < 0.001$; Mann–Whitney U-test. **c**, Schematic diagram for measurement of stress during application of compressive strain. The device is the same as in **a** but uniaxial strain is applied by displacing the left arm with a micromanipulator. **d**, Tissue stress as a function of applied device strain during deformation at low strain rate (0.5% s^{-1}). Different colours indicate different loading and unloading periods. The dashed line indicates the buckling threshold ε_b. Inset: time course of the device strain applied. $N = 16$ biologically independent replicates were obtained. **e**, Comparison of the buckling threshold measured from the transition identified in stress–strain curves and from the maximum tissue strain identified during imaging experiments (Fig. 1e). NS, not significant, $P = 0.23$; Mann–Whitney U-test. **f**, Representative temporal evolution of stress after application of compressive strains of various amplitudes ε_d applied at high strain rate (100% s^{-1}). The stress is normalized to the pre-tension in the tissue before deformation. The representative examples in **f** and data in **g** are derived from $n = 17$ biologically independent experiments. **g**, Fraction of stress recovery at steady state as a function of device strain for deformation applied at high strain rate. The green line shows the behaviour predicted by the rheological model presented in Fig. 4a.

The tissues reached a planar configuration significantly faster after the second application of compressive strain compared with the first (Fig. 4d,e and Supplementary Video 8), confirming that the time necessary to flatten does depend on the tissue's history of deformation. This 'memory' was recapitulated in the model (Fig. 4e(ii)) and results from incomplete relaxation of the viscous element during the period Δt_1.

Conversely, after 6 min of rest at the initial length (Δt_2, Fig. 4c), which is predicted to be sufficient for full relaxation, the time required to become planar was indistinguishable from that during the first compressive period. This demonstrates that the 'memory'

of the past compression was lost during Δt_2 (Fig. 4d,f and Supplementary Video 9).

Pre-tension and stiffness predict the buckling threshold. In our model, the buckling threshold of epithelia ε_b emerges as the ratio between their pre-tension σ_a and their long time-scale stiffness E. By modulating these parameters, epithelia may be able to regulate their buckling threshold to adapt to different developmental and physiological contexts.

To directly test this prediction, we performed experiments in which we altered the ratio between σ_a and E using inhibitors.
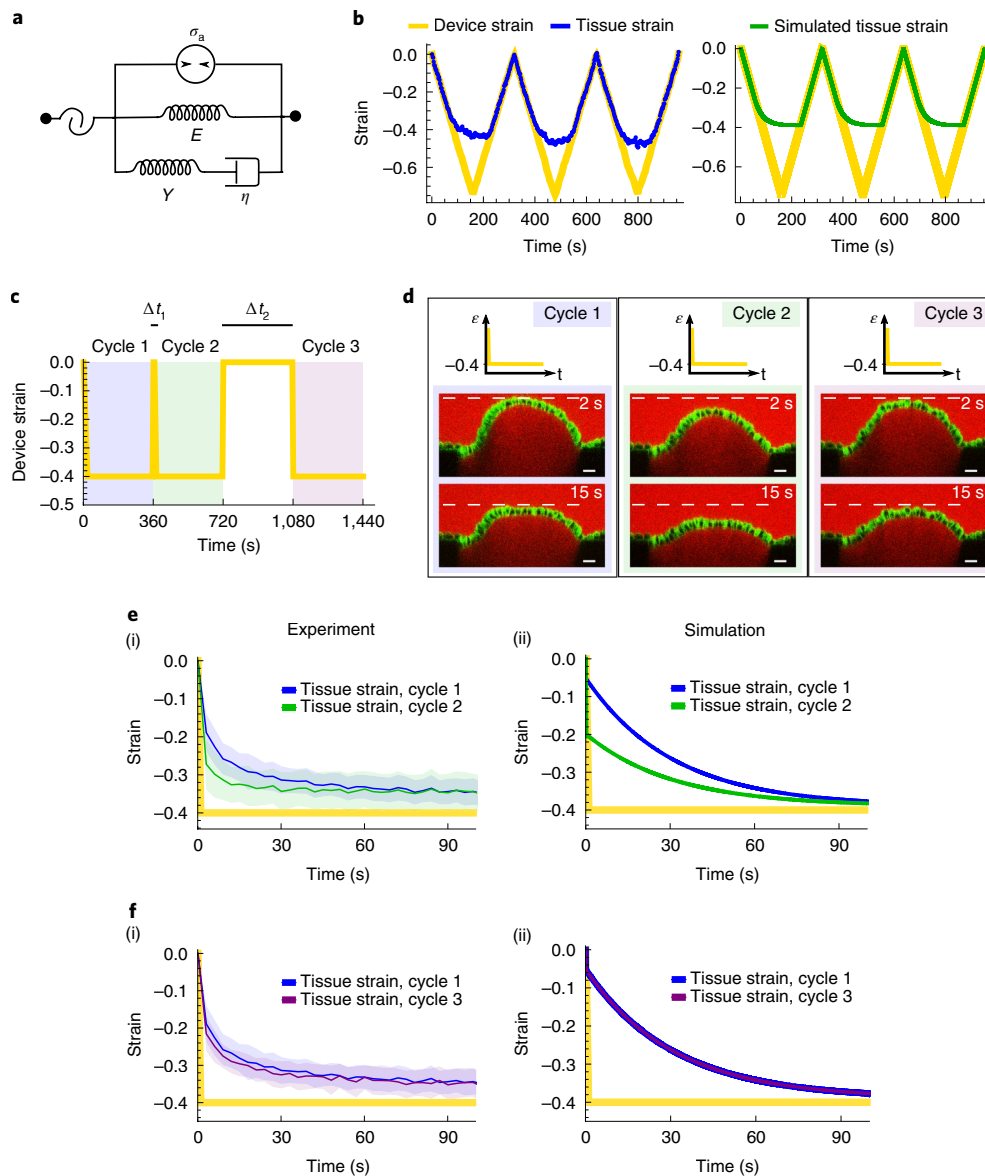
Fig. 4 | Epithelia behave as a pre-tensed viscoelastic material. a, Diagram of the rheological model describing the mechanical response of epithelia to compression. An active element models the contractile stress (σ_a) generated by myosin II. The middle spring (of stiffness E) models the elastic behaviour of the tissue at long timescales, while the spring-dashpot element (of stiffness Y and viscosity η) models the short-time-scale elastic behaviour and viscous relaxation. A condition of loss of stiffness is added in series to model the buckling instability: when the material reaches zero stress, its stiffness becomes null. **b**, Temporal evolution of tissue strain in response to slow cycles of compressive strain (80% amplitude applied at 0.5% s^{-1}, yellow) in a representative experimental dataset and a simulation. The data shows a representative example from $n = 8$ biologically independent experiments. **c**, Sequence of device strain applied to the tissues to assess dependence of the response on strain history. Three cycles of 40% compressive strain were applied, each lasting 6 min. After each cycle the tissue was returned to its original length for a duration $\Delta t_1 = 3$ s (between cycles 1 and 2) and $\Delta t_2 = 6$ min (between cycles 2 and 3). The representative examples in **c**,**d** and data in **e**,**f** are derived from $n = 12$ biologically independent experiments. **d**, Profile images of MDCK monolayers shown 2 s and 15 s after compressive strain application in each of the cycles. For each time point, the dashed white line corresponds to the maximal vertical deflection of the tissue during the first cycle. Scale bars, 20 μm. **e**, Temporal evolution of the tissue strain (mean ± s.d.) after the first (blue) and second (green) cycles of compressive strain (yellow). (i), Experimental data. (ii), Model prediction. **f**, The same as **e** but for the first (blue) and third (purple) cycles of compressive strain.

Since our experiments indicated that both ε_b and σ_a are affected by regulators of contractility, we determined how E depended on actomyosin activity by subjecting MDCK epithelia to a ramp of compressive strain in their quasi-static elastic regime (as in Fig. 3d). The stress–strain curves of treated samples had the same form as controls, consisting of a first regime where stress was proportional to strain, followed by a saturation close to

zero stress at high compressive strain (Fig. 5a). Treatments perturbing myosin activity led to changes in the stiffness E (30% decrease for Y-27632 treatment and 60% increase for calyculin A, Fig. 5b and Supplementary Fig. 6a for paired comparisons) and to comparatively larger changes in pre-tension (45% decrease for Y-27632 and 75% increase for calyculin A, Fig. 3b and Supplementary Fig. 6b for paired comparisons). Thus changes
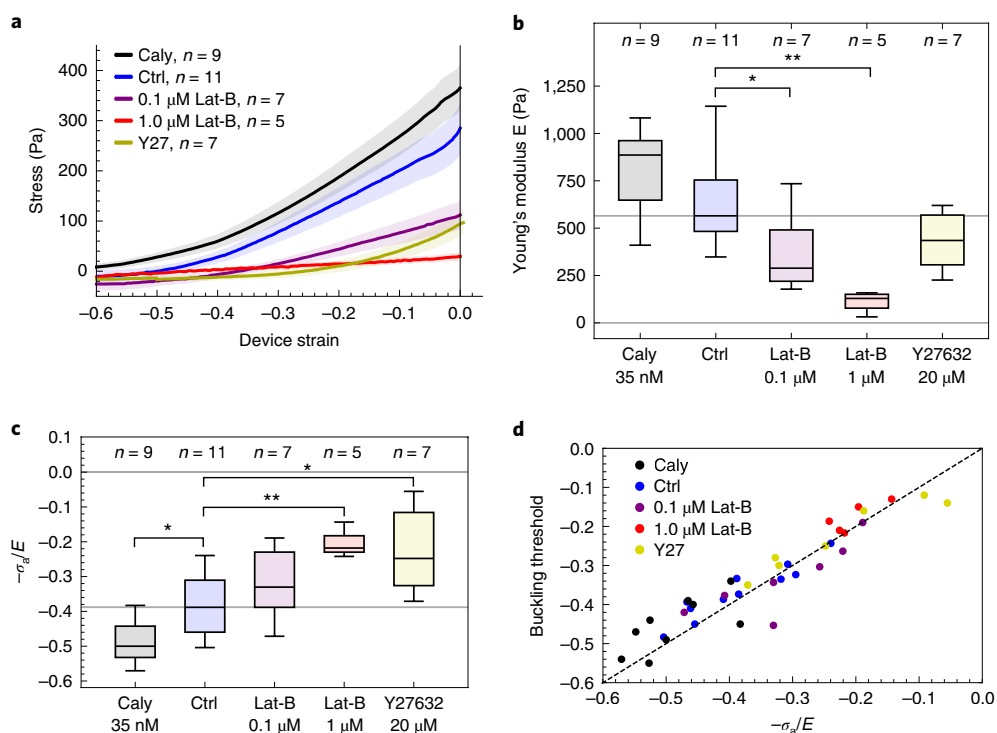
Fig. 5 | Pre-tension and stiffness predict the buckling threshold. a, Tissue stress measured as a function of applied compressive strain for low strain rate (mean ± s.e.m.). Control tissues are shown in blue, tissues treated with 0.1 µM latrunculin-B in purple, 1 µM latrunculin-B in red, 20 µM Y-27632 in yellow and 35 nM calyculin A in black. Note that the strain rate was chosen to ensure that all samples are tested in a quasi-static regime. The number of epithelia examined for each condition is indicated in the figure inset. **b**, Young's modulus E (as a measure of long time-scale stiffness) of the tissues for the same samples as in **a**. Young's modulus was measured from the slope of the curve in **a** before transition to buckling. The horizontal grey line shows the median value for control tissues. In **b** and **c** the distributions' medians, first and third quartiles and ranges are represented by the central bars, bounding boxes and whiskers, respectively. Statistically significant difference, *$P < 0.05$ and **$P < 0.01$, Mann–Whitney U-test. **c**, Ratio $-\sigma_a/E$ corresponding to the buckling threshold predicted by our model for the same samples as in **a**. The horizontal grey line shows the median value for control tissues. **d**, Buckling threshold measured from the transition in the stress–strain curve as a function of the ratio $-\sigma_a/E$ corresponding to the buckling threshold predicted by the model for all control and treated samples as in **a**. The dashed line indicates when these values match.

in σ_a were dominant and the ratio σ_a/E was significantly modified (Fig. 5c). As predicted by our model, the buckling threshold was always very close to the ratio $-\sigma_a/E$ in all conditions even though this ratio was varied by a factor of ~10 across experimental conditions (Fig. 5d). Furthermore, when E and σ_a were decreased by a similar proportion by low-dose latrunculin-B treatment (Fig. 5a–c), the buckling threshold only slightly decreased (Fig. 5a,d and Supplementary Fig. 6c).

Notably, variations in buckling threshold did not correlate with changes in the architecture of the intercellular junctions. High-dose latrunculin-B treatment (1 µM) led to disaggregation of the junctional network leaving only small remnants of junctional F-actin (Supplementary Fig. 6d), whereas Y-27632 did not affect junctional F-actin. However, both treatments caused a similar reduction in buckling threshold. Conversely, in Y-27632 and calyculin A treatments, the buckling threshold was altered in opposite directions without noticeable changes in cell–cell junctions (Supplementary Fig. 6d), suggesting that myosin II activity affects long-term stiffness E indirectly by changing tension within the actin network. Overall, our data show that the ratio $-\sigma_a/E$ derived from our model matches the measured buckling threshold over a wide range of mechanobiological conditions. To provide a full understanding of the phenomenon from the molecular scale up, future work will need to uncover the molecular pathways regulating tissue stiffness and pre-tension.

Outlook

Our results reveal that epithelia can accommodate remarkably large and rapid reductions in surface area. This response to compressive strains arises from isometric cell shape changes and is orchestrated autonomously by the actomyosin cytoskeleton, which not only controls the dynamics of the response but also the transition from planar to folded morphology. We observed identical behaviours in epithelia from different tissues (kidney and skin) and with different organizations (mono- and multi-layered). The full range of behaviours observed could be reproduced by a simple zero-dimensional mechanical model of the epithelium as a pre-tensed viscoelastic sheet that exhibits a buckling instability on reaching compressive stress. Based on this model, we propose that the viscoelastic properties of the tissue set the timescale of the cell shape adaptation that enables flattening. This timescale—of the order of tens of seconds—is commensurate with that of mechanical relaxation observed in *Drosophila*[18,28,29], with the relaxation of stress fibres following nanosurgery[30] and with the turnover rate of the proteins of the actomyosin cytoskeleton[31].

Our results demonstrate that the tissue response possesses a well-defined limit at a compressive strain of ~35%, that is the buckling threshold, above which stable folds can be formed. The close match between the buckling threshold of MDCK and HaCaT epithelia suggests that it is not a tissue-specific property but rather may stem from the bulk properties of actomyosin networks. Indeed, the buckling threshold is regulated by the interplay between myosin

generated pre-tension and tissue elasticity—the ratio of these two quantities defines the strain at which the tissue reaches compressive stress. Although our experiments only consider epithelia devoid of a substrate, our model indicates that the buckling threshold should only be marginally modified by the presence of a thin extracellular matrix such as that found in the lung[32] or many developing tissues undergoing morphogenesis[33,34] (Supplementary Note 4). The buckling instability that we uncover may act in parallel to other well-studied mechanisms of epithelial bending and folding, which include differential growth of connected tissues[7,35] and spatially patterned force generation[36]. Indeed, apical (or basal) constrictions are often preceded in vivo by an increase in cell density before fold formation[2,6], implying that polarized constriction is accompanied by a planar compressive deformation of cells, which could tune tissue folding. Thus, future studies should consider a role for the reduction of tissue pre-tension during epithelial folding.

Together, the buckling threshold and flattening timescale define the maximum strain and strain rate that can be imposed on an epithelium before it becomes subjected to compressive stresses. Such stresses can be damaging to cells[37] and stress accumulation at the epithelium–substrate interface could lead to delamination of the epithelium. The buckling threshold and flattening timescale are therefore crucial material parameters for understanding the response of epithelia to compressive strain during morphogenesis or normal organ physiology. On longer timescales, this underlines the need for cellular-scale mechanisms such as cell delamination in epithelia to counter the deleterious effects of prolonged compression[13,14]. Finally, our results also raise the possibility that actomyosin pre-tension may play a role in various cell[38,39] and tissue contexts throughout evolution to act as a buffer against unwanted stresses and distortions of shape that may otherwise be caused by compression.

Online content

Any methods, additional references, Nature Research reporting summaries, source data, statements of code and data availability and associated accession codes are available at https://doi.org/10.1038/s41563-019-0461-x.

References

1. Tschumperlin, D. J. et al. Bronchial epithelial compression regulates MAP kinase signaling and HB-EGF-like growth factor expression. *Am. J. Physiol. Lung. Cell. Mol. Physiol.* **282**, L904–L911 (2002).
2. Martin, A. C., Kaschube, M. & Wieschaus, E. F. Pulsed contractions of an actin–myosin network drive apical constriction. *Nature* **457**, 495–499 (2009).
3. Shyer, A. E. et al. Emergent cellular self-organization and mechanosensation initiate follicle pattern in the avian skin. *Science* **357**, 811–815 (2017).
4. Etournay, R. et al. Interplay of cell dynamics and epithelial tension during morphogenesis of the Drosophila pupal wing. *eLife* **4**, e07090 (2015).
5. Brodland, G. W. et al. Video force microscopy reveals the mechanics of ventral furrow invagination in Drosophila. *Proc. Natl Acad. Sci. USA* **107**, 22111–22116 (2010).
6. Sidhaye, J. & Norden, C. Concerted action of neuroepithelial basal shrinkage and active epithelial migration ensures efficient optic cup morphogenesis. *eLife* **6**, 1–29 (2017).
7. Shyer, A. E. et al. Villification: how the gut gets its Villi. *Science* **342**, 212–218 (2013).
8. Park, J.-A. et al. Unjamming and cell shape in the asthmatic airway epithelium. *Nat. Mater.* **14**, 1040–1048 (2015).
9. Grainge, C. L. et al. Effect of bronchoconstriction on airway remodeling in asthma. *N. Engl. J. Med.* **364**, 2006–2015 (2011).
10. Tallinen, T. et al. On the growth and form of cortical convolutions. *Nat. Phys.* **12**, 588–593 (2016).
11. Aragona, M. et al. A mechanical checkpoint controls multicellular growth through YAP/TAZ regulation by actin-processing factors. *Cell* **154**, 1047–1049 (2013).
12. Desprat, N., Supatto, W., Pouille, P. A., Beaurepaire, E. & Farge, E. Tissue deformation modulates twist expression to determine anterior midgut differentiation in drosophila embryos. *Dev. Cell* **15**, 470–477 (2008).
13. Eisenhoffer, G. T. et al. Crowding induces live cell extrusion to maintain homeostatic cell numbers in epithelia. *Nature* **484**, 546–549 (2012).
14. Marinari, E. et al. Live-cell delamination counterbalances epithelial growth to limit tissue overcrowding. *Nature* **484**, 542–545 (2012).
15. Wyatt, T., Baum, B. & Charras, G. A question of time: Tissue adaptation to mechanical forces. *Curr. Opin. Cell Biol.* **38**, 68–73 (2016).
16. Étienne, J. et al. Cells as liquid motors: mechanosensitivity emerges from collective dynamics of actomyosin cortex. *Proc. Natl Acad. Sci. USA* **112**, 2740–2745 (2015).
17. Chanet, S. et al. Actomyosin meshwork mechanosensing enables tissue shape to orient cell force. *Nat. Commun.* **8**, 1–13 (2017).
18. Clément, R., Collinet, C., Dehapiot, B., Lecuit, T. & Lenne, P. Viscoelastic dissipation stabilizes cell shape changes during tissue morphogenesis. *Curr. Biol.* **27**, 3132–3142 (2017).
19. Harris, A. R. et al. Characterizing the mechanics of cultured cell monolayers. *Proc. Natl Acad. Sci. USA* **109**, 16449–16454 (2012).
20. Harris, A. R. et al. Generating suspended cell monolayers for mechanobiological studies. *Nat. Protoc.* **8**, 2516–2530 (2013).
21. Wyatt, T. P. J. et al. Emergence of homeostatic epithelial packing and stress dissipation through divisions oriented along the long cell axis. *Proc. Natl Acad. Sci. USA* **112**, 5726–5731 (2015).
22. Salbreux, G., Charras, G. & Paluch, E. Actin cortex mechanics and cellular morphogenesis. *Trends Cell Biol.* **22**, 536–545 (2012).
23. Fischer-Friedrich, E. et al. Rheology of the active cell cortex in mitosis. *Biophys. J.* **111**, 589–600 (2016).
24. Hutson, M. S. et al. Forces for morphogenesis investigated with laser microsurgery and quantitative modeling. *Science* **300**, 145–149 (2003).
25. Valon, L., Marín-Llauradó, A., Wyatt, T., Charras, G. & Trepat, X. Optogenetic control of cellular forces and mechanotransduction. *Nat. Commun.* **8**, 14396 (2017).
26. Tambe, D. T. et al. Collective cell guidance by cooperative intercellular forces. *Nat. Mater.* **10**, 469–475 (2011).
27. Audoly, B. & Pomeau, Y. *Elasticity and Geometry. From Hair Curls to the Non-linear Response of Shells* (Oxford Univ. Press, 2010).
28. Bonnet, I. et al. Mechanical state, material properties and continuous description of an epithelial tissue. *J. R. Soc. Interface* **9**, 2614–2623 (2012).
29. Bambardekar, K., Clément, R., Blanc, O., Chardès, C. & Lenne, P.-F. Direct laser manipulation reveals the mechanics of cell contacts in vivo. *Proc. Natl Acad. Sci. USA* **112**, 1416–1421 (2015).
30. Kassianidou, E., Brand, C. A., Schwarz, U. S. & Kumar, S. Geometry and network connectivity govern the mechanics of stress fibers. *Proc. Natl Acad. Sci. USA* **114**, 2622–2627 (2017).
31. Khalilgharibi, N., Fouchard, J., Recho, P., Charras, G. & Kabla, A. The dynamic mechanical properties of cellularised aggregates. *Curr. Opin. Cell Biol.* **42**, 113–120 (2016).
32. Weibel, E. R. On the tricks alveolar epithelial cells play to make a good lung. *Am. J. Respir. Crit. Care Med.* **191**, 504–513 (2015).
33. Pastor-Pareja, J. C. & Xu, T. Shaping cells and organs in drosophila by opposing roles of fat body-secreted collagen IV and perlecan. *Dev. Cell* **21**, 245–256 (2011).
34. Davidson, L. A., Keller, R. & DeSimone, D. W. Assembly and remodeling of the fibrillar fibronectin extracellular matrix during gastrulation and neurulation in Xenopus laevis. *Dev. Dyn.* **231**, 888–895 (2004).
35. Nelson, C. M. On buckling morphogenesis. *J. Biomech. Eng.* **138**, 021005 (2016).
36. Lecuit, T. & Lenne, P.-F. Cell surface mechanics and the control of cell shape, tissue patterns and morphogenesis. *Nat. Rev. Mol. Cell Biol.* **8**, 633–644 (2007).
37. Kocgozlu, L. et al. Epithelial cell packing induces distinct modes of cell extrusions. *Curr. Biol.* **26**, 2942–2950 (2016).
38. Costa, K. D., Hucker, W. J. & Yin, F. C. P. Buckling of actin stress fibers: a new wrinkle in the cytoskeletal tapestry. *Cell Motil. Cytoskeleton* **52**, 266–274 (2002).
39. Tofangchi, A., Fan, A. & Saif, M. T. A. Mechanism of axonal contractility in embryonic drosophila motor neurons in vivo. *Biophys. J.* **111**, 1519–1527 (2016).

Author contributions

T.P.J.W., J.F., B.B. and G.T.C. designed the experiments. T.P.J.W., J.F., A.L. and N.K. carried out the experiments. T.P.J.W. and J.F. performed the data and image analysis. P.R. and A.J.K. designed the rheological model. T.P.J.W., J.F., B.B. and G.T.C. wrote the manuscript. All authors discussed the results and manuscript.

Competing interests

The authors declare no competing interests.

Additional information

Supplementary information is available for this paper at https://doi.org/10.1038/s41563-019-0461-x.

Reprints and permissions information is available at www.nature.com/reprints.

Correspondence and requests for materials should be addressed to B.B., A.J.K. or G.T.C.

Publisher's note: Springer Nature remains neutral with regard to jurisdictional claims in published maps and institutional affiliations.

Methods

Cell culture. MDCK and HaCaT cells were cultured at 37 °C in an atmosphere of 5% CO_2. Cells were passaged at a 1:5 ratio every 3 to 4 days using standard cell culture protocols and disposed of after 30 passages. For MDCK cells, the culture medium was composed of high glucose DMEM (Thermo Fisher Scientific) supplemented with 10% foetal bovine serum (FBS; Sigma) and 1% penicillin-streptomycin (Thermo Fisher Scientific). MDCK-E-Cadherin-GFP cell lines (described in ref. [20]) were cultured in the same conditions as wild-type cells except that 250 ng ml^{-1} puromycin was added to the culture medium. HaCaT cells were cultured in low calcium conditions, consisting of a minimal DMEM supplemented with 0.03 mM $CaCl_2$, 10% calcium-free FBS, 1% penicillin-streptomycin and 1% L-Glutamine (Gibco).

Fabrication of devices for imaging of tissue response to compression and for stress measurement during compression. For profile imaging of epithelia during compression, tissues were cultured on custom-made imaging devices as described in ref. [21]. Briefly, device arms were made from glass capillaries (Sutter Instruments) and a length of nickel-titanium (nitinol) wire (Euroflex) that acted as a hinge. Glass coverslips (VWR) were glued to the glass capillaries to act as a substrate for cell culture. To allow precise control over both compressive and tensile strains, another small piece of glass capillary was added to the hinged side of the device at an angle to allow continuous contact with the micromanipulator probe (see illustration in Fig. 1a).

The stress measurement devices were an adaptation of the force measurement device described in ref. [20]. Briefly, a nickel-titanium (nitinol) wire was glued into a bent glass capillary. Then, tygon cylinders were glued to the extremities of the capillary and wire. A hinge was added at the base of the rigid rod to control the applied deformation via a motorized micromanipulator while the force was computed from images of the movement of the flexible wire and the stiffness of the flexible wire (see the illustration in Fig. 3a).

Generation of suspended tissues and preconditioning. Suspended monolayers of MDCK cells were generated as described in ref. [19]. Briefly, a drop of collagen was placed between the test rods and left to dry at 37 °C to form a solid scaffold. This collagen was then rehydrated before cells were seeded onto it and cultured for 48–72 h. Immediately before each experiment the collagen scaffold was removed via enzymatic digestion. HaCaT epithelia were made using the same procedure. During the generation of HaCaT epithelia, cells were grown in high calcium culture medium instead of the low calcium medium used for routine culture to allow the formation of robust intercellular junctions.

Before each experiment, the tissues were preconditioned by applying five cycles of 30% stretch at a rate of 1% s^{-1}. The tissues were then left unperturbed for 6 min before application of compressive strain.

Confocal imaging of tissues and mechanical manipulation. Tissues were imaged at 37 °C in a humidified atmosphere with 5% CO_2. The imaging medium consisted of DMEM without phenol red supplemented with 10% FBS. To visualize the shape of the tissue during mechanical manipulation, cell membranes were labelled with CellMask membrane stain for 10 min following the manufacturer protocol (Thermo Fisher Scientific). AlexaFluor-647-conjugated dextran, 10,000 MW (Thermo Fisher Scientific) was added at 20 µg ml^{-1} to the imaging medium to visualize by exclusion the coverslips on which the epithelia were grown.

Profile views of the tissues during mechanical manipulation were obtained using a ×30 objective (UPLSAPO S, numerical aperture 1.05, Olympus) mounted on an Olympus IX83 inverted microscope equipped with a scanning laser confocal head (Olympus FV-1200). Each image consisted of approximately 200 slices spaced by 0.5 µm. Time series were acquired with an interval of ~2 s between frames.

For imaging of cell shape change, cell membranes were visualized with CellMask. Z-stacks were acquired using a ×60 objective (UPLSAPO, numerical aperture 1.3, Olympus) mounted on a spinning disk confocal microscope that consisted of a Yokogawa spinning disk head (CSU22; Yokogawa) and an iXon camera (Andor) interfaced to an IX81 Olympus inverted microscope.

To apply the mechanical deformation during confocal imaging, a custom-made adaptor was wedged in the top end of the hinged arm of the stretching device. The adaptor was connected to a two-dimensional manual micromanipulator mounted on a motorized platform (M-126.DG1 controlled through a C-863 controller, Physik Instrumente). The manual micromanipulators were used for initial positioning of the adaptor. Then, the tissues were deformed by moving the motorized platform that was controlled via a custom-made Labview program (National Instruments).

Quantification of device strain, tissue strain and flattening half-life. To precisely quantify the imposed compressive strain, the positions of the two coverslip edges that delimited the span of suspended tissue were determined by segmentation of dye exclusion in Alexa-647 fluorescence images. The strain imposed by the device was then defined as:

$$\varepsilon_d = \frac{d - l_0}{l_0} \tag{1}$$

where l_0 and d are the coverslip-to-coverslip distances before and after compressive strain, respectively.

To quantify length evolution in images of tissue profiles in response to compression, an implementation of the Chan–Vese algorithm[40] in Mathematica (Wolfram Research) was used to segment the cells from the background. To convert each binary mask generated by segmentation into a line, morphological thinning was applied to the mask repeatedly until complete skeletonization. The length of the shortest path between opposite edges of the image via foreground pixels thus constituted a measure of the cross-sectional contour length of the epithelia (see Supplementary Fig. 1b). The tissue strain at each time point was then defined as:

$$\varepsilon(t) = \frac{l(t) - l_0}{l_0} \tag{2}$$

where l_0 and $l(t)$ are the suspended tissue length before deformation and at time t after application of compressive strain, respectively.

The half-life of tissue strain in response to a step of compression (Fig. 1) was defined as the time necessary for the tissue to decrease its contour length by 50% of the total length change that occurred. This time was extracted after polynomial interpolation of the evolution of tissue strain with time $\varepsilon(t)$.

Quantification of three-dimensional cell shapes. The cell outlines were automatically segmented using the Fiji[41] plugin Tissue Analyser[42]. Segmentation was subsequently verified and corrected manually if necessary. Measurements of cell shape were extracted from the resulting outlines using custom-written routines in Mathematica (Wolfram Research). Cell length measurements were obtained by calculating the minimum bounding box of the cell outline. Bounding boxes were oriented along the experimental x and y axes with the x axis corresponding to the axis of deformation. Measurements of cell height were obtained manually in Fiji from cross-sectional slices through the image stack along y–z planes.

Drug treatments. Drug treatments were performed as follows. To block myosin contractility, blebbistatin was added at a 20 µM concentration for MDCK tissues or 75 µM concentration for HaCaT tissues, 10 min before experiments. To block Rho-kinase activity, Y-27632 was added at a concentration of 20 µM, 10 min before experiments. To increase myosin contractility, phosphatases were inhibited by addition of 35 nM of calyculin A, 10 min before experiments. For complete depolymerization of the F-actin cytoskeleton, we treated tissues with 3 µM latrunculin-B for 30 min before experiments. For dose-dependent depolymerization of junctional F-actin, we treated tissues with either 1 µM or 0.1 µM latrunculin-B for 1 h before experiments.

Mechanical testing experiments. Mechanical testing experiments were performed at 37 °C in Leibovitz's L15 without phenol red (Thermo Fisher Scientific) supplemented with 10% FBS. Tissues were imaged every second using a ×2 objective (2X PLN, Olympus) mounted on an inverted microscope (Olympus IX-71). Images were acquired with a charged-coupled device camera (GS3-U3-60QS6M-C, Pointgrey). Compressive strain was applied using the motorized platform described above.

Stress–strain measurements. To measure the uniaxial stress in the tissue, we measured the deflection of the flexible arm of the device from images before and after detachment of the tissue (see Fig. 3a). The epithelia were detached from the reference arm of the device by cutting them with a tungsten needle.

The force applied by the tissue on the flexible arm can be estimated by considering that the flexible arm acts as a cantilevered beam. We define x_i^w as the position of the wire when the epithelium is attached between the bars and x_0^w as the position of the wire when the epithelium is detached from the bars (the rest position). The force applied by the tissue on the wire is given by:

$$F = k\Delta x^w = k(x_i^w - x_0^w) \tag{3}$$

where k is the stiffness of the wire defined as:

$$k = \frac{3\pi E r^4}{4L^3} \tag{4}$$

Here, E is the Young's modulus of the wire, r its radius and L its length. E was independently measured by loading the wire with pieces of plasticine of different weights and measuring the deflection of the wire as described in ref. [20].

The stress in the tissue was then computed as:

$$\sigma = \frac{F}{wh} \tag{5}$$

where w is the average width of the tissue determined from bright-field images and h the tissue thickness. As shown in Fig. 2a,b, tissue thickness was dependent on the applied strain. Previous work[19] and Fig. 2b show that the cell volume remains constant during changes in tissue area. However, once the buckling threshold ($\varepsilon_b \approx -0.35$) is exceeded, the tissue length does not change and therefore the

thickness also does not change. With these assumptions, we could estimate the evolution of the thickness h for calculation of σ as follows:

$$h_{[\varepsilon > -0.4]} = \frac{h_0}{1 + \varepsilon} \tag{6}$$

and

$$h_{[\varepsilon \leq -0.4]} = \frac{h_0}{1 + \varepsilon_{[h = -0.4]}} \tag{7}$$

In experiments, the deflection of the wire Δx^{w} was determined by image cross-correlation with a subpixel accuracy through a custom-written algorithm based on the register_translation function of scikit-image, a Python image processing toolbox[43]. For the analysis, a portion of the wire was cropped from the images acquired during the experiments. The average error of the stress measurement method was measured from simulated displacements of the cropped region over ten different samples. The deflection obtained via the algorithm was then compared to the deflection applied numerically. The difference found in force was 22 ± 31 nN (mean $\pm$ s.d.), which corresponds to 1.1 ± 1.6 Pa (mean $\pm$ s.d.).

Tissue pre-stress measurements (σ_a) were then obtained from the stress value before any deformation was imposed to the tissue, that is, $\sigma = \frac{F}{wh}$.

For experiments in which tissue strain was varied, the position of the rigid rod $x^{\mathrm{b}}(t)$ was used to compute the displacement applied to the tissue and the flexible rod was used to determine the stress in the epithelium. This position was extracted using the same method as for estimating the position of the flexible wire in pretension measurements. The device strain was defined as:

$$\varepsilon = \frac{\Delta x^{\mathrm{b}} + \Delta x^{\mathrm{w}}}{l_0} \tag{8}$$

where $\Delta x^{\mathrm{b}} = x_i^{\mathrm{b}} - x_0^{\mathrm{b}}$ refers to the displacement of the rigid rod, $\Delta x^{\mathrm{w}} = x_i^{\mathrm{w}} - x_0^{\mathrm{w}}$ is the displacement of the flexible rod and l_0 is the initial rod-to-rod distance.

Note that the deflection of the flexible wire Δx^{w} due to the evolution of tissue stress over time was small compared to the deflection imposed by the movement of the rigid bar Δx^{b}. For example, for a dataset where a deformation of $-54 \pm 5\%$ was applied, the movement of the wire led to a variation in deformation of only $6 \pm 4\%$ over the course of the experiment.

Determination of the buckling threshold from stress–strain curves. Stress–strain curves were biphasic with stress first decreasing linearly with strain before saturating at high compressive strain. The transition strain between the two regimes was determined as follows. For each strain ε_i between $[0, \varepsilon_{\max}]$, we fitted a linear function to the stress σ over the interval $[0, \varepsilon_i]$ and a constant over the interval $[\varepsilon_i, \varepsilon_{\max}]$. For each ε_i, the average of the sum of residuals is computed:

$$R_{[0, \varepsilon_i]} = \frac{1}{N} \sum_{i=1}^{N} \left(\Delta R^2 - (a\varepsilon_i + b) \right)^2 \tag{9}$$

where a and b are fitting parameters and N is the number of data points used for the fit, and

$$R_{[\varepsilon_i, \varepsilon_{\max}]} = \frac{1}{N} \sum_{i=1}^{N} \left(\Delta R^2 - b \right)^2 \tag{10}$$

The transition point is then defined as the strain ε_i that minimizes the sum of the average errors over each interval:

$$R_{\mathrm{tot}}(\varepsilon_t) = \min \left(R_{[0, \varepsilon_i]} + R_{[\varepsilon_i, \varepsilon_{\max}]} \right) \tag{11}$$

The stress at transition was then equal to $\sigma_t = \sigma(\varepsilon_t)$. In addition, the elasticity of the tissue E could be extracted from the slope of the linear portion of curve.

F-actin staining. MDCK Ecadherin-GFP cells were cultured to 90% confluence on glass coverslips. They were fixed with 4% paraformaldehyde diluted in PBS for 20 min at room temperature, permeabilized in 0.2% Triton-X in PBS for 5 min and blocked with a solution of 10% horse serum in PBS for 30 min. To label F-actin, the cells were incubated with a solution of Phalloidin-Alexa-647 diluted at 1:40 from a stock solution of 200 units ml^{-1} for 1 h at room temperature. The samples were then imaged on an Olympus FV-1200 confocal microscope.

Statistical and data analysis. All routine data and statistical analyses were performed using the Python language environment and its scientific libraries (NumPy, SciPy) as well as Mathematica. Image processing was carried out with the Fiji package. All box plots show the median value (central bar), the first and third quartiles (bounding box) and the range (whiskers) of the distribution. All tests of statistical significance are Mann–Whitney U-tests or Wilcoxon signed-rank tests for paired tests, unless otherwise stated. Measured values are given as mean $\pm$ s.e.m. unless otherwise stated. Each dataset is pooled across experiments that were performed on at least 3 separate days. In all box plots, statistically significant difference *$P < 0.05$, **$P < 0.01$ and ***$P < 0.001$. The number of tissues examined in each condition is indicated above each box plot.

Reporting Summary. Further information on research design is available in the Nature Research Reporting Summary linked to this article.

Data availability
The data that support the findings of this study are available from the corresponding authors upon reasonable request.

Code availability
All code created for the analysis of the data in this study is available from the corresponding authors upon reasonable request.

References
40. Chan, T. F. & Vese, L. A. Active contours without edges. *IEEE Trans. Image Process.* **10**, 266–277 (2001).
41. Schindelin et al. Fiji: an open-source platform for biological-image analysis. *Nat. Methods* **9**, 676–682 (2012).
42. Aigouy, B. et al. Cell flow reorients the axis of planar polarity in the wing epithelium of drosophila. *Cell* **142**, 773–786 (2010).
43. van der Walt et al. scikit-image: image processing in Python. *PeerJ* **2**, e453 (2014).

Corresponding author(s):   Guillaume Charras

Reporting Summary

Nature Research wishes to improve the reproducibility of the work that we publish. This form provides structure for consistency and transparency in reporting. For further information on Nature Research policies, see Authors & Referees and the Editorial Policy Checklist.

Statistical parameters

When statistical analyses are reported, confirm that the following items are present in the relevant location (e.g. figure legend, table legend, main text, or Methods section).

n/a	Confirmed	
☐	☒	The exact sample size (n) for each experimental group/condition, given as a discrete number and unit of measurement
☐	☒	An indication of whether measurements were taken from distinct samples or whether the same sample was measured repeatedly
☐	☒	The statistical test(s) used AND whether they are one- or two-sided *Only common tests should be described solely by name; describe more complex techniques in the Methods section.*
☒	☐	A description of all covariates tested
☒	☐	A description of any assumptions or corrections, such as tests of normality and adjustment for multiple comparisons
☐	☒	A full description of the statistics including central tendency (e.g. means) or other basic estimates (e.g. regression coefficient) AND variation (e.g. standard deviation) or associated estimates of uncertainty (e.g. confidence intervals)
☐	☒	For null hypothesis testing, the test statistic (e.g. F, t, r) with confidence intervals, effect sizes, degrees of freedom and P value noted *Give P values as exact values whenever suitable.*
☒	☐	For Bayesian analysis, information on the choice of priors and Markov chain Monte Carlo settings
☒	☐	For hierarchical and complex designs, identification of the appropriate level for tests and full reporting of outcomes
☒	☐	Estimates of effect sizes (e.g. Cohen's d, Pearson's r), indicating how they were calculated
☐	☒	Clearly defined error bars *State explicitly what error bars represent (e.g. SD, SE, CI)*

Our web collection on statistics for biologists may be useful.

Software and code

Policy information about availability of computer code

Data collection	The tissues were deformed by moving a motorized platform via a custom-made Labview program version 2012-SP1 (National Instruments). The LabView code is available upon request.
Data analysis	All other routine data and statistical analysis were performed using the Python language environment and its scientific libraries (NumPy, SciPy) as well as Mathematica version 11.2.0.0 (Wolfram Research). Image processing was carried out with the ImageJ package Fiji. Cell outlines were automatically segmented and hand-corrected using the Fiji plugin Tissue Analyzer. All custom code is available upon request.

For manuscripts utilizing custom algorithms or software that are central to the research but not yet described in published literature, software must be made available to editors/reviewers upon request. We strongly encourage code deposition in a community repository (e.g. GitHub). See the Nature Research guidelines for submitting code & software for further information.

Data

All manuscripts must include a [data availability statement](#). This statement should provide the following information, where applicable:

- Accession codes, unique identifiers, or web links for publicly available datasets
- A list of figures that have associated raw data
- A description of any restrictions on data availability

> The data that support the findings of this study are available from the corresponding
> author upon reasonable request.

Field-specific reporting

Please select the best fit for your research. If you are not sure, read the appropriate sections before making your selection.

☒ Life sciences   ☐ Behavioural & social sciences   ☐ Ecological, evolutionary & environmental sciences

For a reference copy of the document with all sections, see [nature.com/authors/policies/ReportingSummary-flat.pdf](#)

Life sciences study design

All studies must disclose on these points even when the disclosure is negative.

Sample size	Each dataset is pooled across experiments which were performed on at least 3 separate days. Sample size is provided for each experiment. No statistical methods were used to predetermine sample size. The sample size was defined in each case as the maximum possible given our resources.
Data exclusions	Only data from very 'overgrown' tissues were excluded, based on a pre-determined definition of overgrown. For MDCK cells, overgrown monolayers were defined as monolayers that had more than one 'lump' in a field of imaging. A lump is a region where two layers of cells are present. For HaCaT tissues, overgrown tissues are tissues that had more than 3 layers.
Replication	To verify reprodicibility, the experiments were performed on different days and for some experiments with different people. In all experiments described, the same effects were obtained independent of day or experimenter.
Randomization	Samples (tissue monolayers) were allocated randomly into experimental groups on any given experimental day.
Blinding	Blinding was not performed since quantifications were obtained through algorithms which were automated and therefore not susceptible to experimenter bias.

Behavioural & social sciences study design

All studies must disclose on these points even when the disclosure is negative.

Study description	*Briefly describe the study type including whether data are quantitative, qualitative, or mixed-methods (e.g. qualitative cross-sectional, quantitative experimental, mixed-methods case study).*
Research sample	*State the research sample (e.g. Harvard university undergraduates, villagers in rural India) and provide relevant demographic information (e.g. age, sex) and indicate whether the sample is representative. Provide a rationale for the study sample chosen. For studies involving existing datasets, please describe the dataset and source.*
Sampling strategy	*Describe the sampling procedure (e.g. random, snowball, stratified, convenience). Describe the statistical methods that were used to predetermine sample size OR if no sample-size calculation was performed, describe how sample sizes were chosen and provide a rationale for why these sample sizes are sufficient. For qualitative data, please indicate whether data saturation was considered, and what criteria were used to decide that no further sampling was needed.*
Data collection	*Provide details about the data collection procedure, including the instruments or devices used to record the data (e.g. pen and paper, computer, eye tracker, video or audio equipment) whether anyone was present besides the participant(s) and the researcher, and whether the researcher was blind to experimental condition and/or the study hypothesis during data collection.*
Timing	*Indicate the start and stop dates of data collection. If there is a gap between collection periods, state the dates for each sample cohort.*
Data exclusions	*If no data were excluded from the analyses, state so OR if data were excluded, provide the exact number of exclusions and the rationale behind them, indicating whether exclusion criteria were pre-established.*
Non-participation	*State how many participants dropped out/declined participation and the reason(s) given OR provide response rate OR state that no participants dropped out/declined participation.*

Randomization	*If participants were not allocated into experimental groups, state so OR describe how participants were allocated to groups, and if allocation was not random, describe how covariates were controlled.*

Ecological, evolutionary & environmental sciences study design

All studies must disclose on these points even when the disclosure is negative.

Study description	*Briefly describe the study. For quantitative data include treatment factors and interactions, design structure (e.g. factorial, nested, hierarchical), nature and number of experimental units and replicates.*
Research sample	*Describe the research sample (e.g. a group of tagged Passer domesticus, all Stenocereus thurberi within Organ Pipe Cactus National Monument), and provide a rationale for the sample choice. When relevant, describe the organism taxa, source, sex, age range and any manipulations. State what population the sample is meant to represent when applicable. For studies involving existing datasets, describe the data and its source.*
Sampling strategy	*Note the sampling procedure. Describe the statistical methods that were used to predetermine sample size OR if no sample-size calculation was performed, describe how sample sizes were chosen and provide a rationale for why these sample sizes are sufficient.*
Data collection	*Describe the data collection procedure, including who recorded the data and how.*
Timing and spatial scale	*Indicate the start and stop dates of data collection, noting the frequency and periodicity of sampling and providing a rationale for these choices. If there is a gap between collection periods, state the dates for each sample cohort. Specify the spatial scale from which the data are taken*
Data exclusions	*If no data were excluded from the analyses, state so OR if data were excluded, describe the exclusions and the rationale behind them, indicating whether exclusion criteria were pre-established.*
Reproducibility	*Describe the measures taken to verify the reproducibility of experimental findings. For each experiment, note whether any attempts to repeat the experiment failed OR state that all attempts to repeat the experiment were successful.*
Randomization	*Describe how samples/organisms/participants were allocated into groups. If allocation was not random, describe how covariates were controlled. If this is not relevant to your study, explain why.*
Blinding	*Describe the extent of blinding used during data acquisition and analysis. If blinding was not possible, describe why OR explain why blinding was not relevant to your study.*

Did the study involve field work? ☐ Yes ☐ No

Field work, collection and transport

Field conditions	*Describe the study conditions for field work, providing relevant parameters (e.g. temperature, rainfall).*
Location	*State the location of the sampling or experiment, providing relevant parameters (e.g. latitude and longitude, elevation, water depth).*
Access and import/export	*Describe the efforts you have made to access habitats and to collect and import/export your samples in a responsible manner and in compliance with local, national and international laws, noting any permits that were obtained (give the name of the issuing authority, the date of issue, and any identifying information).*
Disturbance	*Describe any disturbance caused by the study and how it was minimized.*

Reporting for specific materials, systems and methods

Materials & experimental systems

n/a	Involved in the study
☒	Unique biological materials
☒	Antibodies
☐	☒ Eukaryotic cell lines
☒	Palaeontology
☒	Animals and other organisms
☒	Human research participants

Methods

n/a	Involved in the study
☒	ChIP-seq
☒	Flow cytometry
☒	MRI-based neuroimaging

Unique biological materials

Policy information about <u>availability of materials</u>

Obtaining unique materials

Describe any restrictions on the availability of unique materials OR confirm that all unique materials used are readily available from the authors or from standard commercial sources (and specify these sources).

Antibodies

Antibodies used

Describe all antibodies used in the study; as applicable, provide supplier name, catalog number, clone name, and lot number.

Validation

Describe the validation of each primary antibody for the species and application, noting any validation statements on the manufacturer's website, relevant citations, antibody profiles in online databases, or data provided in the manuscript.

Eukaryotic cell lines

Policy information about <u>cell lines</u>

Cell line source(s)

The only cell lines used in this study were the MDCK II WT, MDCK II ECad GFP and HaCaT cell lines. The MDCK II WT and MDCK II ECad GFP cell lines are described extensively in Harris et al. 2012. The parental cell line (MDCK II WT) was obtained from Professor Yasuyuki Fujita (Hokkaido University, Japan). The HaCaT cell line was obtained from Professor Karl Matter (UCL, UK).

Authentication

To authenticate the cell lines used, we performed morphology tests and used low cell passage numbers

Mycoplasma contamination

Mycoplasma testing was performed during the course of research using the MycoAlert kit (Lonza). All lines tested negative.

Commonly misidentified lines
(See <u>ICLAC</u> register)

No commonly misidentified cell lines were used in the study.

Palaeontology

Specimen provenance

Provide provenance information for specimens and describe permits that were obtained for the work (including the name of the issuing authority, the date of issue, and any identifying information).

Specimen deposition

Indicate where the specimens have been deposited to permit free access by other researchers.

Dating methods

If new dates are provided, describe how they were obtained (e.g. collection, storage, sample pretreatment and measurement), where they were obtained (i.e. lab name), the calibration program and the protocol for quality assurance OR state that no new dates are provided.

☐ Tick this box to confirm that the raw and calibrated dates are available in the paper or in Supplementary Information.

Animals and other organisms

Policy information about <u>studies involving animals</u>; <u>ARRIVE guidelines</u> recommended for reporting animal research

Laboratory animals

For laboratory animals, report species, strain, sex and age OR state that the study did not involve laboratory animals.

Wild animals

Provide details on animals observed in or captured in the field; report species, sex and age where possible. Describe how animals were caught and transported and what happened to captive animals after the study (if killed, explain why and describe method; if released, say where and when) OR state that the study did not involve wild animals.

Field-collected samples

For laboratory work with field-collected samples, describe all relevant parameters such as housing, maintenance, temperature, photoperiod and end-of-experiment protocol OR state that the study did not involve samples collected from the field.

Human research participants

Policy information about <u>studies involving human research participants</u>

Population characteristics

Describe the covariate-relevant population characteristics of the human research participants (e.g. age, gender, genotypic information, past and current diagnosis and treatment categories). If you filled out the behavioural & social sciences study design questions and have nothing to add here, write "See above."

Recruitment

Describe how participants were recruited. Outline any potential self-selection bias or other biases that may be present and how these are likely to impact results.

ChIP-seq

Data deposition

☐ Confirm that both raw and final processed data have been deposited in a public database such as [GEO](#).

☐ Confirm that you have deposited or provided access to graph files (e.g. BED files) for the called peaks.

Data access links
May remain private before publication.

For "Initial submission" or "Revised version" documents, provide reviewer access links. For your "Final submission" document, provide a link to the deposited data.

Files in database submission

Provide a list of all files available in the database submission.

Genome browser session
(e.g. [UCSC](#))

Provide a link to an anonymized genome browser session for "Initial submission" and "Revised version" documents only, to enable peer review. Write "no longer applicable" for "Final submission" documents.

Methodology

Replicates

Describe the experimental replicates, specifying number, type and replicate agreement.

Sequencing depth

Describe the sequencing depth for each experiment, providing the total number of reads, uniquely mapped reads, length of reads and whether they were paired- or single-end.

Antibodies

Describe the antibodies used for the ChIP-seq experiments; as applicable, provide supplier name, catalog number, clone name, and lot number.

Peak calling parameters

Specify the command line program and parameters used for read mapping and peak calling, including the ChIP, control and index files used.

Data quality

Describe the methods used to ensure data quality in full detail, including how many peaks are at FDR 5% and above 5-fold enrichment.

Software

Describe the software used to collect and analyze the ChIP-seq data. For custom code that has been deposited into a community repository, provide accession details.

Flow Cytometry

Plots

Confirm that:

☐ The axis labels state the marker and fluorochrome used (e.g. CD4-FITC).

☐ The axis scales are clearly visible. Include numbers along axes only for bottom left plot of group (a 'group' is an analysis of identical markers).

☐ All plots are contour plots with outliers or pseudocolor plots.

☐ A numerical value for number of cells or percentage (with statistics) is provided.

Methodology

Sample preparation

Describe the sample preparation, detailing the biological source of the cells and any tissue processing steps used.

Instrument

Identify the instrument used for data collection, specifying make and model number.

Software

Describe the software used to collect and analyze the flow cytometry data. For custom code that has been deposited into a community repository, provide accession details.

Cell population abundance

Describe the abundance of the relevant cell populations within post-sort fractions, providing details on the purity of the samples and how it was determined.

Gating strategy

Describe the gating strategy used for all relevant experiments, specifying the preliminary FSC/SSC gates of the starting cell population, indicating where boundaries between "positive" and "negative" staining cell populations are defined.

☐ Tick this box to confirm that a figure exemplifying the gating strategy is provided in the Supplementary Information.

Magnetic resonance imaging

Experimental design

Design type

Indicate task or resting state; event-related or block design.

Design specifications	*Specify the number of blocks, trials or experimental units per session and/or subject, and specify the length of each trial or block (if trials are blocked) and interval between trials.*
Behavioral performance measures	*State number and/or type of variables recorded (e.g. correct button press, response time) and what statistics were used to establish that the subjects were performing the task as expected (e.g. mean, range, and/or standard deviation across subjects).*

Acquisition

Imaging type(s)	*Specify: functional, structural, diffusion, perfusion.*
Field strength	*Specify in Tesla*
Sequence & imaging parameters	*Specify the pulse sequence type (gradient echo, spin echo, etc.), imaging type (EPI, spiral, etc.), field of view, matrix size, slice thickness, orientation and TE/TR/flip angle.*
Area of acquisition	*State whether a whole brain scan was used OR define the area of acquisition, describing how the region was determined.*

Diffusion MRI ☐ Used ☐ Not used

Preprocessing

Preprocessing software	*Provide detail on software version and revision number and on specific parameters (model/functions, brain extraction, segmentation, smoothing kernel size, etc.).*
Normalization	*If data were normalized/standardized, describe the approach(es): specify linear or non-linear and define image types used for transformation OR indicate that data were not normalized and explain rationale for lack of normalization.*
Normalization template	*Describe the template used for normalization/transformation, specifying subject space or group standardized space (e.g. original Talairach, MNI305, ICBM152) OR indicate that the data were not normalized.*
Noise and artifact removal	*Describe your procedure(s) for artifact and structured noise removal, specifying motion parameters, tissue signals and physiological signals (heart rate, respiration).*
Volume censoring	*Define your software and/or method and criteria for volume censoring, and state the extent of such censoring.*

Statistical modeling & inference

Model type and settings	*Specify type (mass univariate, multivariate, RSA, predictive, etc.) and describe essential details of the model at the first and second levels (e.g. fixed, random or mixed effects; drift or auto-correlation).*
Effect(s) tested	*Define precise effect in terms of the task or stimulus conditions instead of psychological concepts and indicate whether ANOVA or factorial designs were used.*

Specify type of analysis: ☐ Whole brain ☐ ROI-based ☐ Both

Statistic type for inference (See Eklund et al. 2016)	*Specify voxel-wise or cluster-wise and report all relevant parameters for cluster-wise methods.*
Correction	*Describe the type of correction and how it is obtained for multiple comparisons (e.g. FWE, FDR, permutation or Monte Carlo).*

Models & analysis

n/a	Involved in the study
☐	☐ Functional and/or effective connectivity
☐	☐ Graph analysis
☐	☐ Multivariate modeling or predictive analysis

Functional and/or effective connectivity	*Report the measures of dependence used and the model details (e.g. Pearson correlation, partial correlation, mutual information).*
Graph analysis	*Report the dependent variable and connectivity measure, specifying weighted graph or binarized graph, subject- or group-level, and the global and/or node summaries used (e.g. clustering coefficient, efficiency, etc.).*
Multivariate modeling and predictive analysis	*Specify independent variables, features extraction and dimension reduction, model, training and evaluation metrics.*